JOURNAL OF OPTOELECTRONICS AND ADVANCED MATERIALS Vol. 12, No. 5, May 2010, p. 980 - 993

# A WKB interpolation-Wavelet method for 3-D Numerical simulation of nanoscale FinFET Photodetector including quantum mechanical effects

R. RAMESH, M. MADHESWARAN[a], K. KANNAN[b]
*Department of Electronics and Communication Engineering, M.A.M College of Engineering, Trichy – 621 105, TamilNadu, India*
[a]*Center for Advanced Research, Muthayammal Engineering College, Rasipuram, TamilNadu, India*
[b]*Department of Mathematics, SASTRA University, Thanjavur, TamilNadu, India*

In this paper, a three dimensional numerical modeling of an optically controlled nanoscale FinFET considering quantum mechanical effects has been theoretically examined and analyzed. The device characteristics are obtained from the self-consistent solution of 3D Poisson-Schrödinger equation using WKB (Wentzel Kramers Brilloin) interpolation-Wavelet method. This method provides more accurate results by dynamically adjusting the computational mesh and scales the CPU time linearly with the number of mesh points using oscillating interpolation derived from WKB asymptotics, hence reducing the numerical cost. The results obtained for dark and illuminated conditions are used to examine the performance of the device for its suitable use as a photodetector.

(Received March 1, 2010; accepted May 26, 2010)

*Keywords*: Nanoscale FinFET photodetector, Quantum mechanical effects, WKB-Wavelet, Schrödinger equation

## 1. Introduction

The photosensitivity and the integrated circuit compatibility of Field-Effect Transistors (FETs) have extended potential of these devices for their use as photodetectors. Among the FETs configuration, Metal Semiconductor Field Effect Transistor (MESFET) and High Electron Mobility Transistor (HEMT) have been studied theoretically as well as experimentally by several workers for various optically-controlled applications [1-5]. A three dimensional modeling of a nano MISFET photodetector without including quantum mechanical effects [6] has been reported. A transition from bulk to multiple-gate fully depleted (FD) silicon-on-insulator (SOI) offers drive current and better short-channel immunity [7]. CMOS designs below 0.1μm are severely constrained by SCE and gate insulator tunneling [8-11].One of the approaches to circumvent the gate tunneling restriction is to change the device structure so that the MOSFET gate length can be further scaled even with thicker oxide. Double-gate MOSFET (DGFET) is one of the most promising devices for channel length in the range 10-30 nm [12-15]. The alignment of the top and bottom gates to each other and to source/drain (S/D) doping is crucial to device performance, because misalignment may cause extra gate-to-S/D overlap capacitance as well as S/D series resistance [16].In order to optimize the performance of double gate devices, self-aligned processes and structures are proposed, with FinFET being one of the most promising [17-21]. The FinFET is a symmetric three-gate structure, which means that all its three gates have the same work function and also at the same potential. This three dimensional (3-D) structure requires 3-D analysis. The potential variation in the channel used to calculate the subthreshold current and threshold voltage of FinFETs with doped and undoped channels has been reported [22]. Two dimensional (2-D) models can only be used to study the operation of the device along certain plane sections of the channel. An analytical model based on 3-D analysis for an undoped channel has been reported [23].El Hamid et al., [24] presented the 3-D analytical modeling including mobile charge term. W. Yang et al., [25] reported the scaling theory of FinFET by 3-D analytical solution of Poisson's equation in channel region. The existing literatures reported on analytical modeling have shown the complexity in evaluating various device characteristics including QM effects. In addition, it has been found that many assumptions and approximations have to be incorporated while the device is analytically modeled. Quantum mechanical modeling is important for many reasons, e.g., the tunneling current through ultra-thin gate oxide adds to the low limit of the off-state current [26].In FinFET devices, quantum effects and non-equilibrium, ballistic or near-ballistic transport has large impact on device performance [26]. For channel length comparable to the carrier scattering length, carriers transport ballistically. The inversion layer thickness cannot be treated same along the channel [26]. An analytical charge model based on self-consistent solution of Poisson's and Schrödinger equation for 3-D FinFETs is carried out [27]. A ballistic quantum-mechanical simulation using CBR

(Contact Block Reduction) method to investigate the behavior of 10nm FinFET device is reported [28].Double-gate FinFET devices with symmetric and asymmetric poly-silicon gates have been fabricated [29]. FinFET is developed with special emphasis on process simplicity and compatibility with conventional CMOS technology [30].A simple capacitive model was proposed by [31] to predict the relationship between DIBL and S swing. N. Ben Abdallah proposed the modeling of ballistic quantum transport in nanostructures using the decomposition of the wave function with reduced simulation time [32].A numerical scheme for the 1-D Schrödinger equation used to simulate a resonant tunneling diode uses the oscillating interpolating function from WKB asymptotic [33]. A 3-D quantum simulation of silicon nanowire transistors with the effective mass approximation using mode space approach producing high computational efficiency is proposed [34]. In this paper, a 3D numerical model for n-channel nanoscale FinFET photodetector including QME has been developed and presented. The prime focus is to obtain the device characteristics, considering QM effects by numerically solving the 3D Poisson- Schrödinger equations using Wavelet and WKB approximation until self-consistency is achieved. The WKB approximation is a more efficient method for approximation of the device parameters. When solving the Poisson-Schrödinger equations with standard finite element or finite difference methods require a large number of grid points thus increasing unnecessarily the numerical cost. The basic idea of this method is that rather than using polynomial interpolation functions, oscillating interpolation functions provided by WKB approximation are used. This reduces the numerical cost of the simulation and produces more accurate results with much coarser grids. This method provides a very good performance in terms of CPU time savings and fast convergence, since at each step; the evaluation of grid refinement does not require computations introducing significant overhead.

## 2. Physics based modeling

The general FinFETs structure is shown in Fig.1. The following are the geometrical parameters.

i) Gate Length ($L_g$): The physical gate length of FinFETs, defined by spacer gap.

ii) Fin Height ($H_{fin}$): The height of silicon fin, defined by the distance between the top gate and buried oxide layer (BOX).

iii) Fin Width ($T_{fin}$): The thickness of silicon fin, defined between the front and back gates.

iv) Top gate thickness ($T_{ox1}$): The thickness of the top gate oxide.

v) Front or back gate thickness ($T_{ox2}$): The thickness of the front or back gate oxide.

vi) Channel Length ($L_{eff}$): The channel length is estimated by the metallurgical junction for abrupt junctions.

Geometrical channel width defined as W=2x $H_{fin}$ + $T_{fin.}$

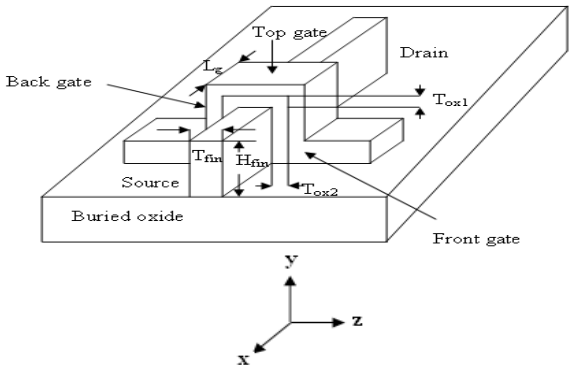


*Fig. 1. Schematic diagram of FinFET.*

Obviously, when $T_{fin}$ is much larger than $H_{fin}$ or when top gate oxide is much thinner than the front and back oxides, FinFET can be treated as single-gate fully depleted SOI MOSFET (FDFET) as long as the silicon fin remains fully depleted [23]. When $H_{fin}$ is much larger than $T_{fin}$ or top gate oxide ($T_{ox1}$) is much thicker than the front and back oxides ($T_{ox2}$), FinFET can be treated as DGFET [23].It is difficult to assume a simple potential distribution because of its asymmetric 3-D structure. The electrostatic potential in the subthreshold region can be described by the 3-D Poisson's equation.

$$\frac{\partial^2 U(x,y,z)}{\partial x^2}+\frac{\partial^2 U(x,y,z)}{\partial y^2}+\frac{\partial^2 U(x,y,z)}{\partial z^2}=\frac{-q[N_a(x,y,z)+n(x,y,z)-p(x,y,z)]}{\varepsilon_s}+\Delta n \tag{1}$$

where $U(x,y,z)$ is the surface potential at a particular point $(x,y,z)$, $N_a(x,y,z)$ is the uniform channel doping concentration, q is the electronic charge, $\varepsilon_s$ is the permittivity of silicon $n(x,y,z)$ is the electron concentration, $p(x,y,z)$ is the hole concentration, Δn is the excess carriers generated per unit volume.

$$n(x,y,z)=\sum_{j=1}^{2}\sum_{i=1}^{\infty} n_{ij}\left|\psi(x,y,z)\right|^2 \tag{2}$$

where $i$ is the valley and $j$ is the subband.

$$n_{ij}=\frac{n_{vj}m_{dj}k_BT}{\pi\hbar^2}\ln\left[1+\exp\left(\frac{E_{Fn}-E_{ij}}{k_BT}\right)\right] \tag{3}$$

Based on the Fermi-Dirac statistics, the electron concentration can be expressed as

$$n(x,y,z)=\sum_{j=1}^{2}\sum_{i=1}^{\infty}\frac{1}{\pi\hbar}\sqrt{2m^{*}k_{B}T}F_{-1/2}\left(\frac{E_{Fn}-E_{ij}}{k_{B}T}\right)\left|\psi(x,y,z)\right|^{2} \tag{4}$$

where $\psi(x,y,z)$ is the wave function and $F_k$ is the Fermi-Dirac integrals of order k. These integrals are defined as

$$F_k(\eta)=\frac{1}{\Gamma(k+1)}\int_0^{\infty}\frac{u^k\,du}{1+e^{u-\eta}},\ k\geq -1$$

and also have the following property

$$\frac{d}{d\eta}F_k(\eta)=F_{k-1}(\eta),k\leq -1$$

The six boundary conditions are set by the top gate, front gate, back gate, source, and drain and buried oxide (Fig.1). The buried oxide is assumed to be thick enough that any finite potential across the buried oxide leads to a negligible electric field. The boundaries between gate oxide and silicon fin are eliminated by replacing the physical dimensions with effective dimensions. The whole region is treated as homogenous silicon with effective thickness ($T_{eff}$), effective channel length ($L_{eff}$) and effective height ($H_{eff}$) [25]. Because, in the short channel device, the lateral electric field becomes comparable to the normal electric field, the geometrical average method should be adopted [23] to reduce errors. These two effective parameters are defined by [25]

$$T_{eff}=\sqrt{T_{fin}\times\left(T_{fin}+\frac{4\varepsilon_{si}}{\varepsilon_{ox}}T_{ox2}\right)} \tag{5}$$

$$H_{eff}=\sqrt{H_{fin}\times\left(H_{fin}+\frac{2\varepsilon_{si}}{\varepsilon_{ox}}T_{ox1}\right)} \tag{6}$$

where $\varepsilon_{ox}$ is silicon-oxide permittivity. With all the assumptions and approximations above, the boundary conditions are simplified as [25]

Top Gate:

$$U\Big|_{y=H_{eff}}=V_g-V_{fb.} \tag{7}$$

Front Gate:

$$U\Big|_{z=-T_{eff}/2}=V_g-V_{fb.} \tag{8}$$

Back Gate:

$$U\Big|_{z=T_{eff}/2}=V_g-V_{fb.} \tag{9}$$

Source:

$$U\Big|_{x=0}=V_{bi}+V_{op} \tag{10}$$

Drain:

$$U\Big|_{x=L_{eff}}=V_{bi}+V_{ds}+V_{op} \tag{11}$$

Bottom gate:

$$U\Big|_{y=-H_{eff}}=V_g-V_{fb.} \tag{12}$$

Due to the symmetrical structure in the z direction, the buried oxide boundary condition at the bottom $\frac{\partial U}{\partial z}\Big|_{y=0}=0$ is replaced with the bottom gate boundary condition. where $V_{op}$ is the photo induced voltage.

The excess carriers generated per unit volume due to the absorption of incident optical power density are given by [6]

$$\Delta n=\frac{1}{W_m}\int_0^{W_m}G_{op}(x)\tau_L\,dy \tag{13}$$

where $W_m$ is the maximum width of the depletion layer and is given by

$$W_m=[4\varepsilon_s\ln(N_a/n_i)/q\beta N_a]^{1/2} \tag{14}$$

where $N_a$ is the acceptor concentration. $G_{op}(x)$ is the excess carrier generation rate at any point x in the semiconductor and is given by

$$G_{op}(x)=\frac{p_{opt}}{h\gamma}(1-R_m)(1-R_i)(1-R_s)\alpha e^{-\alpha y} \tag{15}$$

where $P_{opt}$ is the incident optical power density, $h$ is the Planck's constant, $\gamma$ is the operating frequency, $\alpha$ is the absorption coefficient of the semiconductor at the operating wavelength, $R_m, R_i and R_s$ are the reflection coefficient at the metal gate entrance, gate-insulator interface and the insulator-semiconductor interface respectively.

The mean lifetime of the minority carriers in the illuminated condition, $\tau_l$ can be written as

$$\tau_l=(n_i/n_i+\Delta n)\tau \tag{16}$$

where $\tau$ is the lifetime of the carriers for the intrinsic semiconductor. The characteristics of the device in the absence of illumination can be obtained in a similar way by substituting $P_{opt}$=0 in equation (15).

The photo response drain current is given by

$$I_{ph} = I_{DL} - I_{D(DARK)} \tag{17}$$

The photocurrent gain is given by

$$M = I_{ph} / I_L \tag{18}$$

where $I_L$ is the primary current and is given by

$$I_L = q(P_{opt} / h\gamma)A \tag{19}$$

The responsivity of the device, R is defined as the output current divided by the incident light power

$$R = I_{ph} / P_{opt} \tag{20}$$

where $I_{ph}$ is the output current of the photodetector in response to light and $P_{opt}$ is the optical power incident on the photodetector.

External quantum efficiency is defined as the number of carriers collected by the number of incident photons.

$$\eta = (I_{ph} / q) / (P_{opt} / h\gamma) \tag{21}$$

where $I_{ph}$ is the photodetector current generated in response to incident light, q is the electron charge, $P_{opt}$ is the incident optical power in watts, the quantity hγ is the energy per photon in joules, where h is Planck's constant and γ is frequency.

**Model for quantum mechanical ballistic transport**

The 3D effective mass Schrödinger equation along the n-channel is given by [26]

$$\left[ \frac{\hbar^2}{2m_x^*}\frac{\partial^2}{\partial x^2} + \frac{\hbar^2}{2m_y^*}\frac{\partial^2}{\partial y^2} + \frac{\hbar^2}{2m_z^*}\frac{\partial^2}{\partial z^2} + qU_{(x,y,z)} \right] \psi_{x,y,z} = E\,\psi_{x,y,z} \tag{22}$$

In the above equation $m_x^*$, $m_y^*$, $m_z^*$ are effective masses in the x, y and z directions. E is the eigen energy, ħ is the reduced Planck's constant, q is the charge of an electron U(x, y, z) is the surface potential, ψ(x, y, z) is the eigen wave function.

By using the variable separation method and applying the WKB approximation for $\psi$ in the x-direction, the value for $\psi(x, y, z)$ is equated to

$$\psi(x, y, z) = X(x)\phi(y, z) = e^{jk_x x}\phi(y, z) \tag{23}$$

By using the above equation, a plane wave solution in the x-direction is assumed. The

3-D Schrödinger equation reduces to two dimensional Schrödinger equation [26] as follows

$$\frac{\hbar^2}{2m_x^*}\frac{\partial^2}{\partial x^2}\left[e^{ik_x x}\varphi(y, z)\right] = \frac{-\hbar^2}{2m_x^*}k_x^2 e^{ik_x x}(\varphi(y, z)) \tag{24}$$

The equation (24) can be written as

$$\left[\frac{\hbar^2 k_x^2 z}{2m_x^*} - \frac{\hbar^2}{2m_y^*}\frac{\partial^2}{\partial y^2} - \frac{\hbar^2}{2m_z^*}\frac{\partial^2}{\partial z^2} - qU(x, y, z)\right]e^{ik_x x}\varphi(y, z) = Ee^{ik_x x}\varphi(y, z) \tag{25}$$

The above equation (25) can be reduced as follows

$$\left[-\frac{\hbar^2}{2m_y^*}\frac{\partial^2}{\partial y^2} - \frac{\hbar^2}{2m_z^*}\frac{\partial^2}{\partial z^2} - qU(x, y, z)\right]\varphi(y, z) = \left(E - \frac{\hbar^2 k_x^2}{2m_x^*}\right)\varphi(y, z) \tag{26}$$

The following notations are used to indicate the x-dependence. $\psi_x(y, z) = \phi(y, z)$,

$$U_x(y, z) = U(x, y, z)$$

and

$$E_{t,x} = E - \hbar^2 k_x^2 / 2m_x^*.$$

$$E - \frac{\hbar^2 k_x^2}{2m_x^*} = E_{t,x} \tag{27}$$

The 2-D Schrödinger equation (27) is written as

$$\left[-\frac{\hbar^2}{2m_y^*}\frac{\partial^2}{\partial y^2} - \frac{\hbar^2}{2m_z^*}\frac{\partial^2}{\partial z^2}\right]\psi^i_{x(y,z)} - qU_x(y, z)\psi^i_x(y, z) = E^i_{t,x}\psi^i_x(y, z) \tag{28}$$

$$E_{t,x} = E - \frac{\hbar^2 k_x^2}{2m_x^*} = E_t(x) \tag{29}$$

The above equation (29) can be written in the form

$$HX(x) = EX(x)$$

where $H$ is the Hamiltonian operator and $E$ is the energy-eigen value

For Quantum model, the above equation takes the form

$$\hat{H}\,X(x) = \hat{E}\,X(x) \tag{30}$$

Let

$$\hat{H} = \hat{T} + \hat{U} \tag{31}$$

$\hat{T} = K.E = \frac{1}{2}mv^2$ is the kinetic energy of electron and $\hat{P} = mv$ is the potential energy of electron.

$\hat{T}$ can be written as

$$\hat{T} = \frac{1}{2}mv^2 = \frac{1}{2m}(mv)^2 \tag{32}$$

$$\hat{T} = \frac{1}{2m}\hat{P}^2 \tag{33}$$

where $\hat{P}$ is the momentum operator and $\hat{P} = i\hbar\frac{\partial}{\partial x}$

Equation (33) modifies into

$$\hat{T} = \frac{-\hbar^2}{2m_x^*}\frac{\partial}{\partial x^2} \text{ and } U = U(x) \tag{34}$$

Now the value of $\hat{H}$ modifies into

$$\hat{H} = \frac{-\hbar^2}{2m_x^*}\frac{\partial^2}{\partial x^2} + U(x) \tag{35}$$

Multiplying on both side of equation (35) with $\psi(x)$ and substituting in equation (30) we get

$$\left[\frac{-\hbar^2}{2m_x^*}\frac{\partial^2}{\partial x^2} + U(x)\right]\psi(x) = E\psi(x) \tag{36}$$

The equation (36) is the one dimensional Schrödinger's equation and can be written as

$$HX(x) = \left[\frac{-\hbar^2}{2m_x^*}\frac{\partial}{\partial x^2} + E_t(x)\right]X(x) = EX(x) \tag{37}$$

where $X(x) = \psi(x)$ and $E_t(x) = U(x)$

In the above equations, $m_x^*$ $m_y^*$, $m_z^*$ are the effective masses. $\psi_x^i(y,z)$ is the eigen-wave function and $E_{t,x}^i$ is the eigen-energy along a direction. The superscript $i$ is the index of sidebands. The 2-D Schrödinger equation is solved for every point along the channel. The electron effective mass is different in Si and $SiO_2$ region. To find the values of $m_y^*$, $m_z^*$ we assume that the channel is along [100] direction and there are three set of energy valleys in the $k_y$ - $k_z$ plane with different combinations of $m_y^*$, $m_z^*$ and each set has two valleys. For this particular case, the two sets of valleys are collapsed into one with four valleys. Hence there are two sets of different combinations of $m_y^*$, $m_z^*$[26]. Fig.2 shows the constant energy valleys in k-space for silicon, showing six conduction band valleys in [100] direction. The long axis of the ellipsoid corresponds to longitudinal effective mass of electrons and the short axis corresponds to transverse effective mass. For [100] silicon, we have taken two longitudinal valleys with $m* = m_t$ and four transverse valleys with $m* = \sqrt{m_l m_t}$. The above equation (37) is solved using open boundary conditions.

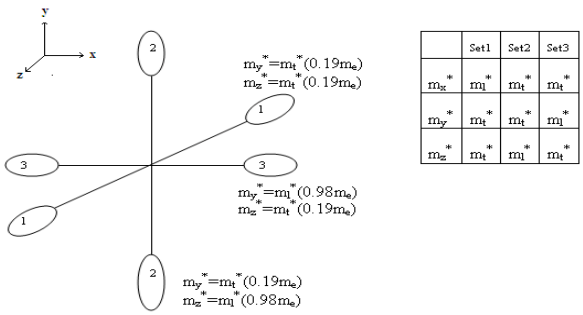


*Fig. 2. Equi-energy valleys in k-space for silicon*

### 3. Multiresolution analysis and wavelets

For semiconductor device simulation using partial differential equations, the grid generation is very important. Grid points must be present accurately approximate to any physical quantity to be measured. The grid layout should be chosen carefully since the computational cost grows with the number of grid points. The difficulty in semiconductor device simulation is due to the different mesh sizes between substrate and doped regions. Finer mesh is needed in doped regions and junctions and coarse mesh for substrate regions, to reduce the number of unknowns and also the simulation time. Hence wavelets with MRA concept are used to achieve this goal. The Wavelet-Galerkin method uses the finite difference method with grid refinement. So, instead of letting the magnitude of wavelet coefficients to choose the basis function in Galerkin approach, let the same coefficients choose which grid points to choose [45].

MRA is an important concept in wavelet theory. Many useful orthonormal wavelets are constructed within this framework. In order to give a good explanation of the relationship between MRA and wavelet basis, a brief summary of Daubechies wavelets are given [46, 47]. The usefulness of wavelets for solving partial differential equations relies on the definition of MRA. An MRA is based on two fundamental concepts: nested subspaces and

orthonormal bases. The first decomposes the information into different scales; the second allows stable and fast algorithms. The space of square integral functions on the real line is denoted by $L^2(R)$. The orthonormal basis of wavelets of $L^2(R)$ is formed by dilations and translations of a single function $\Psi(x)$, called a mother wavelet.

The orthonormal basis of wavelets of $L^2(R)$ is formed by dilations and translations of a single function $\Psi(x)$, called a mother wavelet.

$$\Psi_{jk}(x) = 2^{j/2}\Psi(2^j x - k),\ j,k \in Z. \tag{38}$$

The function $\Psi(x)$ has a companion, the scaling function $\varphi(x)$ .They both satisfy the following two-scale relation

$$\varphi(x) = \sum_k a_k \varphi(2x - k), \tag{39}$$

$$\Psi(x) = \sum_k (-1)^k a_{1-k}\varphi(2x-k), \tag{40}$$

where the coefficients $a_k (k = 0,1,..L-1)$ appearing in the two-scale relations (39) and (40) are called the wavelet filter coefficients. The support of the scaling function $\varphi$ is the interval $[0, L-1]$ while that of the corresponding wavelet $\Psi$ is the interval $[1 - L/2, L/2]$.

**WKB-Wavelet solution for one dimensional Schrödinger's equation**

The one dimensional Schrödinger's equation as given in (37) is

$$-\left[\frac{\hbar^2}{2m_x^*}\frac{\partial^2}{\partial x^2} + qU_{(x)}\right]\psi_x = E\psi_x \tag{41}$$

where $m_x^*$ is the effective mass of an electron in the x direction. E is the eigen energy, ħ is the reduced Planck's constant, q is the charge of an electron U(x) is the surface potential, ψ(x) is the eigen wave function. The 1-D Schrödinger equation can be solved using open boundary conditions.

In [39] the authors have presented a WKB scheme using the continuous finite element method. Let us assume that the nodal values $\psi_n, \psi_{n+1}$ at nodes $x_n, x_{n+1}$ of the wave function $\psi(x)$ are known. Standard linear interpolation gives inaccurate solution on a coarse grid for a grid $I_j$. In order to enhance the accuracy on a coarse grid, the WKB approximation is used to construct a new interpolation function [34].

$$\psi(x) \approx \frac{A}{\sqrt[4]{2m(E-U(x))}}e^{iS(x)} + \frac{B}{\sqrt[4]{2m(E-U(x))}}e^{-iS(x)} \tag{42}$$

where A and B are constants and $S(x)$ is a dimensionless action.

$$S(x) = \frac{\sqrt{2m}}{\hbar}\int_{x_0}^{x}\sqrt{E-U(s)}\ ds$$

$x_0$ is an integration constant. Equation (42) shows the asymptotic behavior of the wavefunction as $\hbar \to 0$ or $E \to \infty$. This asymptotic has two advantages: it is a good approximation not only at higher frequencies but also for slowly varying potentials. The wavefunction is the sum of two terms, each of them being the product of an oscillatory function and a slowly varying one.
The WKB interpolated function is given by [34]

$$\tilde{\psi}(x) = \frac{A_n}{\sqrt[4]{2m(E-U(x))}}e^{iS(x)} + \frac{B_n}{\sqrt[4]{2m(E-U(x))}}e^{-iS(x)}, \ x \in I_n \tag{43}$$

$$I_n = [x_n, x_{n+1}]$$

$$\psi_n = \tilde{\psi}(x_n) = \frac{A_n}{\sqrt[4]{2m(E-U(x_n))}}e^{iS(x_n)} + \frac{B_n}{\sqrt[4]{2m(E-U(x_n))}}e^{-iS(x_n)} \tag{44}$$

$$\psi_{n+1} = \tilde{\psi}(x_{n+1}) = \frac{A_n}{\sqrt[4]{2m(E-U(x_{n+1}))}}e^{iS(x_{n+1})} + \frac{B_n}{\sqrt[4]{2m(E-U(x_{n+1}))}}e^{-iS(x_{n+1})} \tag{45}$$

$$\tilde{\psi}(x) = \alpha_n(x) f_n(x)\psi_n + \beta_n(x) f_{n+1}\psi_{n+1},\ x \in I_n \tag{46}$$

where $\alpha_n$ and $\beta_n$ are the WKB-basis functions given by

$$\alpha_n(x) = -\frac{\sin S_{n+1}(x)}{\sin \gamma_n},\ \beta_n(x) = -\frac{\sin S_n(x)}{\sin \gamma_n}$$

with

$$S_n(x) = \frac{\sqrt{2m}}{\hbar}\int_{x_n}^{x}\sqrt[4]{E-U(s)}\ ds\ ;$$

$$\gamma_n = \frac{\sqrt{2m}}{\hbar}\int_{x_n}^{x_{n+1}}\sqrt[4]{E-U(s)}\ ds$$

and the amplitude factor

$$f_n \text{ is } f_n(x)=\sqrt[4]{\frac{E-U(x_n)}{E-U(x)}}$$

$\sqrt[4]{\ }$ denotes the complex square root with non-negative imaginary part.

For detailed expressions of finding values of $A_n, B_n, S_n(x)$ and $U(s)$ refer [28].

Introducing wavelets in equation (46) gives

$$\alpha_n(x) f_n(x)\psi_n + \beta_n(x) f_{n+1}\psi_{n+1} = \sum_k d_{j,k}\Psi_{j,k}(x) \quad (47)$$

where $d_{j,k}$ is the wavelet coefficient.

$$\beta_n(x) f_{n+1}\psi_{n+1} = -\alpha_n(x) f_n(x)\psi_n + \sum d_{j,k}\Psi_{j,k}(x) \quad (48)$$

$$\beta_n(x) f_{n+1}\psi_{n+1} = -\alpha_n(x) f_n(x)\psi_n + \sum d_{j,k}2^{j/2}\varphi(2^j x-k), k \in Z \quad (49)$$

Equation (49) can be simplified into

$$\beta_n(x) f_{n+1}\psi_{n+1} = -\alpha_n(x) f_n(x)\psi_n + \sum d_{j,k}\varphi_{jk}(x) \quad (50)$$

where k=2-M, 3-M… $2^j$-1 are $2^j$+M-2 are unknown coefficients. $j$ fixes the level of resolution. The larger the value of $j$, the more accurate a solution can be obtained. The parameter $M$ represents that the wavelet associated with the set of $M$ Daubechies filter coefficients is used as a solution bases.

Substituting the wavelet series approximation $\Psi(x)$ for $\psi(x)$ in equation (41) yields [48]

$$-\left[\frac{\hbar^2}{2m_x^*}\frac{d^2}{dx^2}\left(-\alpha_n(x) f_n(x)\psi_n\right)+\sum_k d_{j,k}\varphi_{j,k}(x)+(qU(x)-E)(-\alpha_n(x) f_n(x)\psi_n)+\sum_k d_{j,k}\varphi_{j,k}(x)\right]=0 \quad (51)$$

$$-\left[\frac{\hbar^2}{2m_x^*}\left(-\alpha_n(x) f_n(x)\psi_n\right)+\sum_k d_{j,k}\frac{d^2}{dx^2}\varphi_{j,k}(x)+(qU(x)-E)(-\alpha_n(x) f_n(x)\psi_n)+\sum_k d_{j,k}\varphi_{j,k}(x)\right]=0 \quad (52)$$

To determine the coefficient $d_{j,k}$, we take the inner product of both sides of equation with $\varphi_{jn}$.

$$-\left[\frac{\hbar^2}{2m_x^*}\left(-\alpha_n(x) f_n(x)\psi_n\right)+\sum_k d_{j,k}\int_0^{L_{eff}}\varphi''_{jk}(x)\varphi_{jn}(x)+(qU(x)-E)(-\alpha_n(x) f_n(x)\psi_n)+\sum_k d_{j,k}\int_0^{L_{eff}}\varphi_{jk}(x)\varphi_{jn}(x)\right]=0 \quad (53)$$

For simplicity, we define the following notations for integrals appearing in equation (53)

$$a_{kn}^j=\int_0^{L_{eff}}\varphi_{jk}(x)\varphi_{jn}(x)=\Gamma_{k-n}^0(2^j-n)-\Gamma_{k-n}^0(-n),$$

$$c_{kn}^j=\int_0^{L_{eff}}\varphi''_{jk}(x)\varphi_{jn}(x)=2^{2j}\left[\Gamma_{k-n}^2(2^j-n)-\Gamma_{k-n}^2(-n)\right],$$

The equation (53) becomes

$$-\left[\frac{\hbar^2}{2m_x^*}\left(-\alpha_n(x) f_n(x)\psi_n\right)+\sum_k d_{j,k}C_{kn}^j+(qU(x)-E)(-\alpha_n(x) f_n(x)\psi_n)+\sum_k d_{j,k}a_{kn}^j\right]=0 \quad (54)$$

$$n=2-M,3-M,\ldots 2^j-1$$

$$absolute\,error=|U_{exactsolution}-U_{WKB-Wavelet}| \quad (55)$$

The equation (54) is solved using Cholesky's decomposition method by taking the matrix-vector form of the equation and an accurate value of the surface potential, U(x) is found.

The drain current $I_D$ considering scattering effects is given by [25, 27]

$$I_D = \frac{Wqn_i(V_{gs} - V_T)(1 - \exp\left(-\frac{V_{ds}}{V_T}\right)}{\left[\frac{1}{\upsilon_T} + \frac{1}{D_{eff}/\ell}\right]\int_0^L \frac{dx}{\int_{-H_{fin}/2}^{H_{fin}/2}\int_{-T_{fin}/2}^{T_{fin}/2} \exp\left[\frac{U(x)}{V_T}\right]dydz}} \quad (56)$$

where $\upsilon_T = \sqrt{2K_BT/\pi m^*}$ is the thermal velocity and is independent of the Fermi level. $D_{eff} = (K_BT/q)\mu_{eff}$ is the diffusion coefficient. For low $V_{ds}$, the critical length $\ell \to L$, the channel length. Assuming that only the lowest side band is occupied, the effective mass is $m* = m_t = 0.19m_0$ which gives a thermal velocity $\upsilon_T = 1.2\times10^7 cm/s$. By Mathiessen's rule $\mu_{eff}^{-1} = \mu_0^{-1} + \mu_B^{-1}$ where $\mu_B = \frac{qL}{m*\pi\upsilon_T}$ is the ballistic mobility and $\mu_0 = \frac{q\lambda}{m*\pi\upsilon_T}$ is the low field mobility, $\lambda$ is the mean free path, $W = T_{fin}$ is the width of the device.

The subthreshold swing $S$ is a measure of the gate control on the channel. It can be expressed as

$$S = \frac{\partial V_{gs}}{\partial \log I_{DS}}$$

$$S = \frac{\ln 10}{\beta} \times \frac{1}{1 - 2\Gamma_{11}e^{-\alpha} \times Sin\frac{\pi(x_c + a + c)}{a_{eff}} \times Sin\frac{\pi(y_c + b + d)}{b_{eff}}} \quad (57)$$

In which $\beta$ and $\alpha$ are defined as

$$\beta = \frac{q}{KT}$$

$$\alpha = L_{eff}/2\lambda_{11} = L_{eff}/2\Lambda$$

$$a_{eff} = 2(a + c);\ b_{eff} = 2(b + d)$$

$$a = T_{fin}/2;\ b = H_{fin};\ c = T_{eff}/2 - a;\ d = H_{eff} - b$$

$$\frac{1}{\lambda^2_{mn}} = \left(\frac{m\pi}{a_{eff}}\right)^2 + \left(\frac{n\pi}{b_{eff}}\right)^2$$

$$\Gamma_{mn} = \frac{16}{mn\pi^2}$$

$x_c$ and $y_c$ describe the position of the leakage path in the fin cross section. $x_c$ could be set to zero due to symmetry, while $y_c$ is determined by the geometrical features, doping concentration, and applied voltages. Practically, $y_c$ is treated as a fitting parameter. Substituting $y_c = H_{fin}$ in equation (50) becomes a lower limit of subthreshold swing. $V_{ds}$ is set as 0.05 V, and the lateral electric field along the channel is moderate. Hence, the drift-diffusion is accurate to describe the subthreshold conduction in FinFETs [21].

The electric field along the x direction is given as [6]

$$E_x = \frac{U(i+1) - U(i-1)}{\left(2L/m_x\right)} \quad (58)$$

where $m_x$ are the separation of the grid line along the x direction. $U(i)$ is the surface potential at a particular point and L is the gate length.

The transconductance is a partial derivative of drain current with respect to the gate-source voltage keeping drain-source voltage constant. It is a measure of device gain.

$$g_m\{V_{gs}(i)\}V_{ds,const} = \frac{I_{ds}(i+1) - I_{ds}(i-1)}{V_{gs}(i+1) - V_{gs}(i-1)} \quad (59)$$

The threshold voltage ($V_{th}$) rolloff is given by [25]

$$\Delta V_{th} = -\alpha\frac{Sq}{2.3KT}\exp\left(\frac{-L_{eff}}{2L_d}\pi\right)\left[\sqrt{V_{bi}(V_{bi} - V_{ds}) - |V_{bi}|}\right] \quad (60)$$

$$L_d = \frac{1}{\sqrt{\left(\frac{a}{T_{eff}}\right)^2 + \left(\frac{b}{H_{eff}}\right)^2}}$$

$L_d$ is the drain potential decay length, $V_{bi}$ is the built-in potential, equal to about half of the Si band gap. Equation (60) shows that the $V_{th}$ roll-off is an exponential function of $\frac{L_{eff}}{L_d}$. $V_{th}$ roll-off caused by DIBL is estimated by the necessary gate voltage change in the most leaky path $(x_c, y_c)$ [23]. If the channel furthest away from the gates, i.e., $x_c = T_{eff}/2, y_c = 0$, is chosen as the most leaky path, the sine and cosine terms will be reduced to 1.

## 4. Computational technique

The 3D Poisson's equation (1) using the boundary conditions (7-12) is solved numerically using Leibmann's iteration method to determine the approximate surface potential under illumination for a fixed value of gate voltage and assumed value of drain voltage. This value of surface potential is given to the 3D Schrödinger equation (22). The 3-D Schrödinger equation is then reduced to 1-D equation using separation of variables and WKB approximation. This 1-D Schrödinger equation (36) is solved using WKB interpolation–Wavelet method and the exact value of surface potential is obtained. The drain current can be estimated by numerically integrating the equations (56) using Simpson's one-third rule. The subthreshold swing, electric field, transconductance and

threshold voltage roll-off values are estimated using equations (57,58,59, 60).The results obtained are validated with commercial device simulator results.

**Algorithm**

1. Assign gate length, channel length, device width, height and thickness of silicon.
2. Apply bias voltages and $P_{opt}$ values .
3. Determine numerically the surface potential under illumination by solving the 3D Poisson's equation using boundary conditions.
4. Substitute this surface potential value in the 3D Schrödinger's equation.
5. Reduce 3-D Schrödinger's equation to 1-D equation using variable-separation method and WKB approximation.
6. Solve 1-D Schrödinger's equation numerically using open boundary conditions.
7. Estimate the exact value of surface potential at every point along the channel length.
8. Obtain subthreshold swing, drain characteristics, Mobility, electrical characteristics.

## 5. Results and discussion

Numerical computation has been carried out for the nanoscale FinFET. The parameters used for the calculation are given in Table. 1.

*Table.1. Parameters and constants*

| Parameter | Value |
|---|---|
| Gate Length ($L_g$) | 60 nm |
| Top gate oxide thickness ($T_{ox1}$) | 5 nm |
| Front (or) back gate thickness ($T_{ox2}$) | 1 nm |
| Channel Length ($L_{eff}$) | 60 nm |
| Thermal Voltage ($V_T$) | 0.025852 V |
| Intrinsic carrier concentration ($n_i$) | 9.65 x $10^9$/$cm^3$ |
| Acceptor concentration ($N_a$) | 1 x $10^{16}$/ $cm^3$ |
| Flatband voltage ($V_{fb}$) | -0.48 V |
| Built-in potential ($V_{bi}$) | 0.6 V |
| Gate voltage ($V_g$) | 0.2V |

Fig.3.shows the potential profile of the FinFET including QM effects obtained using WKB interpolation-Wavelet method on a grid of 20 x 13 x 10 points is compared with the reference solution obtained from DAVINCI simulator (broken line). The surface potential $U(x)$ is calculated for different values of $x$ .The WKB interpolation-Wavelet method shows good agreement with the reference values and gives more accurate values due to quantum mechanical effects. The results are validated with DAVINCI results for $V_{DS}$=1.5V under dark condition. The surface potential values under illuminated conditions are calculated for $P_{opt}$=0.5W/$m^2$ and $V_{DS}$=1.5V. It is also found that the surface potential increases with illumination. This is due to the fact that excess carriers generated due to illumination increases the conductivity of the channel. Fig.4.shows the three dimensional surface potential of nanoscale FinFET along channel length and device width including quantum mechanical effects for $V_{ds}$=0.8V. The device width is taken to be equal to channel width (W). The S-factor, which is a measure of the subthreshold behavior of the device, is extracted from the $I_{ds}$-$V_{gs}$ characteristics of the FinFET device. The S-factor for various channel lengths and fin thickness for a constant fin height are obtained from the device simulation and shown in Fig.5.The calculated subthreshold swing (S) is 71.56mV/dec at $V_{ds}$ = 1.5V. This is due to the fact that the punch-through is successfully interrupted by the thin body of FinFET. It is found that the S-factor increases exponentially with decreasing channel length. It is also found that the subthreshold swing increases with illumination. From Fig.6 it is observed that as the $H_{fin}$ is increased from 20 to 100 nm, the saturation of $S$ is observed [23]. The critical $H_{fin}$ needed for saturation is different for devices with different $T_{fin}$ [23]. In Fig.7, $S$ changes more rapidly as $T_{fin}$ changes from 10 to 60 nm, the rate of change increases initially and then slow down. At high $V_{ds}$ values, the electric field will increase at the back surface compared to the top surface. The position of the most leaky path is highly dependent on the channel doping, gate bias and device geometry. For the case of undoped channel and deep subthreshold operation, the device geometry is the dominant variable. The closer the channel path to the gate, the more source barrier is reduced by the gate, while for the channel away from the gate, the more source barrier is reduced by the source/ drain potential [23]. If the source/drain potential penetration is the dominant factor in determining the source barrier, the most leaky path will be the channel path away from the gate. The source/drain potential includes the built-in potential, $V_{bi}$ and applied drain bias, $V_{ds}$ [24].

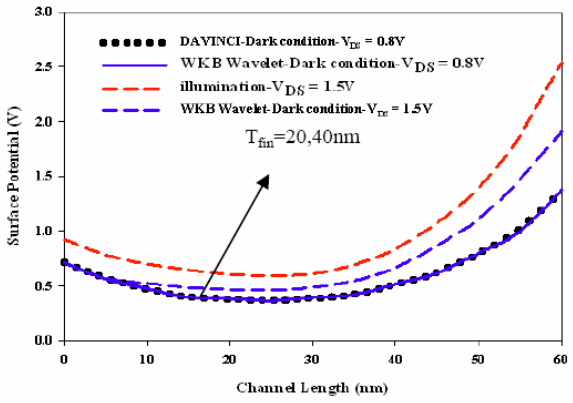


*Fig. 3. Three dimensional potential variation along the channel length under dark and illuminated conditions. $V_g$ = 0.2V, $H_{fin}$ = 60nm, $T_{fin}$ = 20nm, $L_{eff}$ = 60nm, $V_{DS}$=1.5V. The dotted lines show DAVINCI simulated values at $V_{ds}$ = 0.8V [18].*

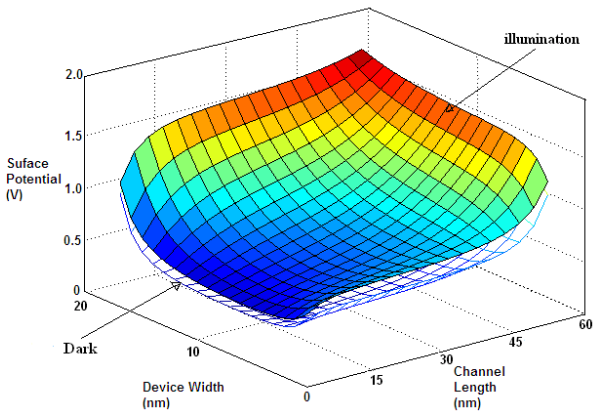


*Fig. 4. Surface potential distribution along the channel length and device width for $V_{DS}$=0.8V, $P_{opt}$=0.5W/m$^2$.*

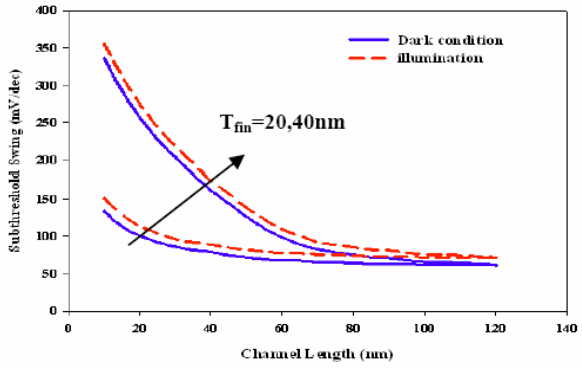


*Fig. 5. Subthreshold swing along channel length for various $T_{fin}$ values at $H_{fin}$= 60nm and $V_{DS}$=1.5V, $P_{opt}$=0.5W/m$^2$.*

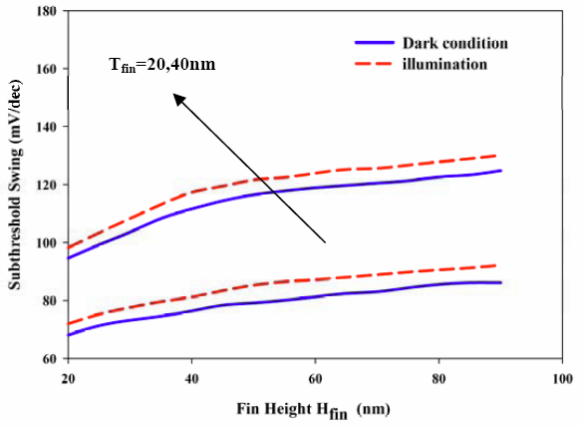


*Fig. 6. Subthreshold Swing for different $T_{fin}$ values, $L_{eff}$=60nm, $V_{DS}$=1.5V, $P_{opt}$=0.5W/m$^2$.*

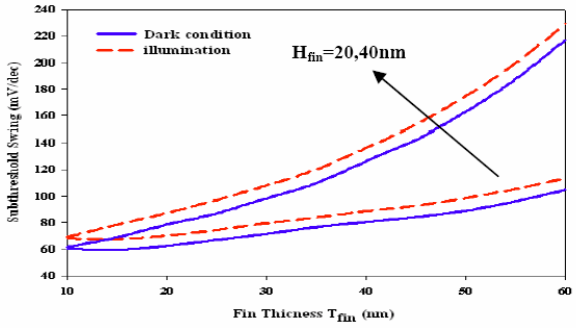


*Fig.7. Subthreshold swing for various $H_{fin}$ values, $L_{eff}$=60nm, $V_{DS}$=1.5V, $P_{opt}$=0.5W/m$^2$.*

The simulated $I_d - V_{gs}$ characteristics are shown in Fig. 8 & 9. The drain current normalized by the channel width $W$ at the same $V_{gs}$ is almost independent of $H_{fin}$ while fixing $T_{fin}$ . The small differences in the normalized drain current with same $H_{fin}$ and different $T_{fin}$ come from the threshold voltage roll-off due to increase in $T_{fin}$[23]. The normalized drain current of FinFET with 10nm $H_{fin}$ is almost twice that of FinFET with 30nm $H_{fin}$ [23]. Depending on the relative ratio of $T_{fin}$ to $H_{fin}$, either one of these two parameters can be the dominant parameter controlling the short channel effects (SCE) of FinFET. For a given $L_{eff}$, changing the dominant parameter will lead to big changes in $V_{th}$ roll-off and subthreshold swing (S) values, while changing the nondominant parameter will result in small changes or almost no changes. This is because the channel is controlled by two gates on the sides while only one gate on the top and no gate at the bottom. In both cases, the effect of illumination increases the drain current.

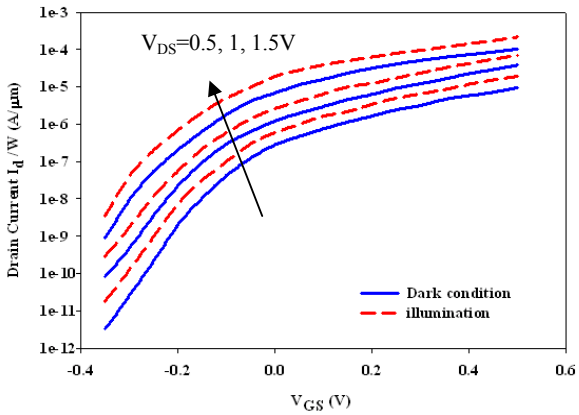


*Fig. 8. $I_d - V_{gs}$ characteristics of FinFET for various $T_{fin}$ values, $P_{opt}$=0.5W/m$^2$ .*

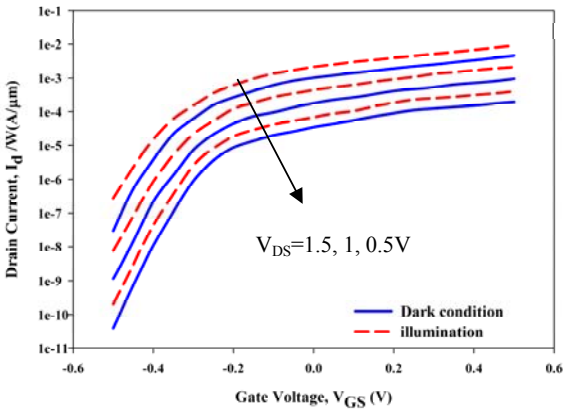


*Fig. 9. $I_d$ –$V_{gs}$ characteristics of FinFET for various $H_{fin}$ values, $P_{opt}$=0.5W/m$^2$.*

The $I_d$-$V_d$ characteristics of nanoscale FinFET are shown in Fig.10. It shows that the subthreshold leakage current is well suppressed even at low doping concentration (1x10$^{16}$ cm$^{-3}$). It is also found that there is no kink effect, which is produced due to floating body. It is shown that for the applied gate-to-source voltage, the drain current also significantly increases. The channel width is determined by applied gate-to-source voltages. The charge carriers pass through the channel and hence the conduction takes place. When the drain voltage is further increased, more charge carriers try to pass through the channel, resulting in an increase in drain current. But these charge carriers passes through the channel width that is created earlier. Hence the drain current saturates after a certain limit even if the drain voltage is increased further. The drain current under illuminated condition is higher than dark condition due to generation of excess carriers under illumination.

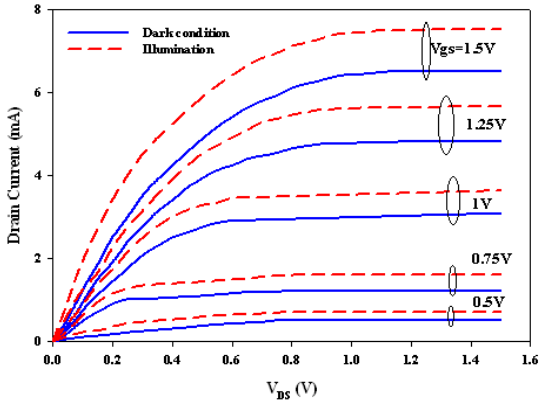


*Fig. 10. Drain current characteristics of FinFET for various $V_{gs}$ values. $T_{fin}$=20nm, $H_{fin}$=60nm, $P_{opt}$=0.5W/m$^2$.*

The transconductance with the applied gate-to-source voltage, for $V_{ds}$=1.5V is shown in Fig.11. Due to the applied voltage and excess carrier generation, photo voltage is induced in the channel. This induced photovoltage decreases the transconductance of photodetector under illumination along the channel.

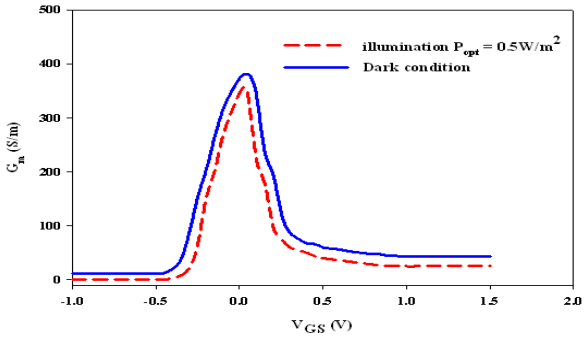


*Fig. 11. Transconductance for $T_{fin}$=20nm, $H_{fin}$=60nm, $V_{ds}$=1.5V, $P_{opt}$=0.5W/m$^2$.*

The distribution of electric field along the channel length is depicted in Fig.12.The electric field along the channel length increases due to QM effects. The electric field increases slowly near the source end and rapidly near the drain end. This is due to the fact that the carrier density near the drain end experiences a rapid decrease in surface concentration which calls for a rapid increase in the electric field to maintain a constant drain current. It is seen that the electric field near the drain end in the illuminated condition is less compared to that in the dark condition. As a result a high drain voltage is needed to attain saturation in the illuminated condition. When the device gets illuminated, more and more electron hole pairs are generated and more crowded. This reduces the mobility of the charge carriers [6].

The distribution of mobility of electrons along the channel due to scattering effects is shown in Fig.13. It is seen that the mobility gets reduced under illuminated condition in comparison with the mobility under dark condition. As more charge carriers are generated under illuminated condition, their mobility gets affected as there is not much free space for their movement.

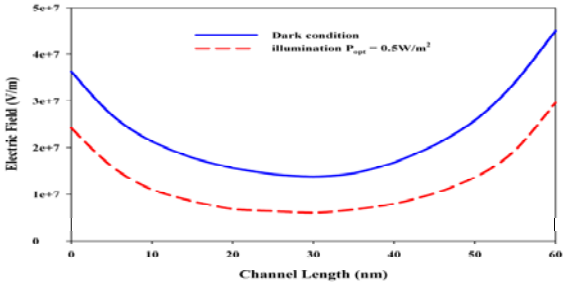


*Fig. 12. Electric Field along channel length for $T_{fin}$=20nm, $H_{fin}$=60nm, $V_{ds}$=1.5V, $P_{opt}$=0.5W/m$^2$.*

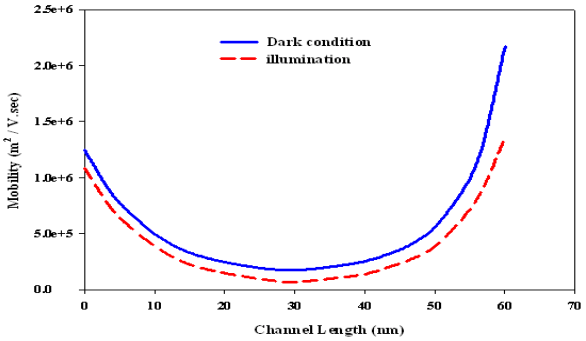


*Fg. 13. Mobility distribution along channel length.*

The variation of photocurrent gain with the incident optical power density for constant applied gate voltage and drain voltage is shown in Fig. 14. It is seen from the figure that the gain decreases with increase in optical power density. This is because of the larger change in the primary photocurrent with the change in the optical power density as compared to the drain photocurrent.

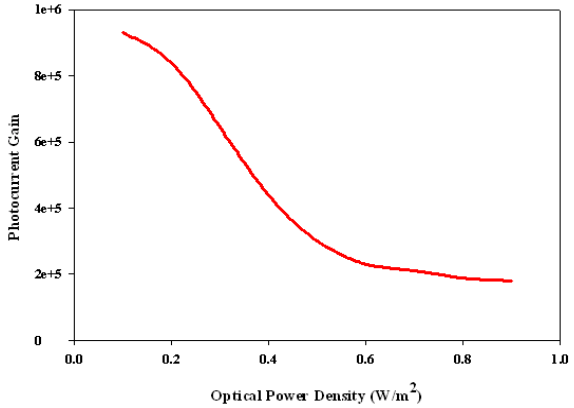


*Fig.14. Variation of photocurrent gain for various optical power density*

Fig. 15 & 16 shows the efficiency of the WKB-Wavelet method by plotting the point wise relative errors of the WOFDM & WKB-Wavelet methods with respect to the Taurus simulated values (reference solution) for the surface potential. The grids are chosen as (20×13×10) for both the WOFDM & WKB-Wavelet methods.

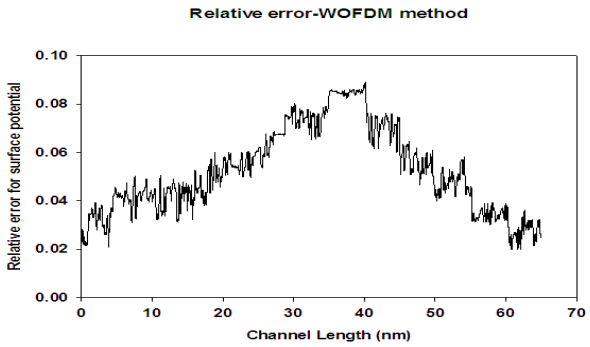


*Fig. 15. Relative error of the WOFDM method (20×13×10 points) with the reference solution (Taurus) for the surface potential.*

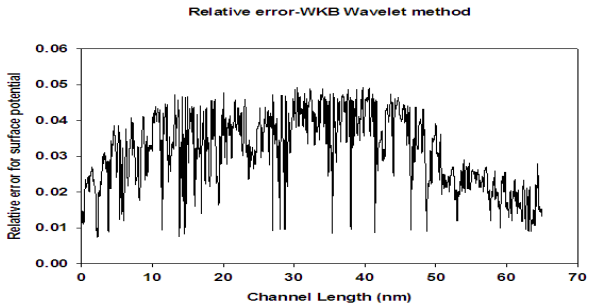


*Fig. 16. Relative error of the WKB-Wavelet method (20×13×10 points) with the reference solution (Taurus) for the surface potential.*

## Numerical efficiency

Table.2 shows that different mesh grid points are used in the transport direction for the resolution of Poisson-Schrödinger equation in order to compute accurate solution. For a 20×13×10 mesh the WOFDM method is nearly 10 times more accurate than the FDM method with considerable reduction in simulation time. The Poisson-Schrödinger equations are solved on the coarser grid (15 grid points). Then the results for the finer grids are interpolated from the coarse ones. This multi-grid procedure enables to use the advantages of WKB approximation and Wavelet for obtaining better solution of the coupled Poisson-Schrödinger equation with reduction in simulation time. The relative error for surface potential is computed with reference to the Taurus simulator values. The simulation time is the total simulation time. The simulation is done using Matlab version 7.0.1 with a personal computer using Intel Dual Core Processor. It is found that the simulation time and the relative error reduces considerably with the WKB-Wavelet method.

*Table.2. Comparisons of the simulation times & mean relative errors of FDM & WKB-Wavelet for different meshes*

| No. of grid points in *x,y,z* | Simulation time WKB-Wavelet | Mean rel. error WKB-Wavelet | Simulation time FDM | Mean rel. error FDM |
|---|---|---|---|---|
| 20×13 ×10 | 102s | 0.0223 | 116 s | 0.2158 |
| 45 × 32 × 23 | 642 s | 0.0165 | 712 s | 0.1635 |
| 60 × 49 × 34 | 1568 s | 0.0083 | 1824 s | 0.0674 |

*Table.3. Comparison of the simulation times & means relative errors of WOFDM & WKB-Wavelet for different meshes*

| No. of grid points *x,y,z* | Simulation Time WKB-Wavelet | Mean rel. error WKB-Wavelet | Simulation Time WOFDM | Mean rel. error WOFDM |
|---|---|---|---|---|
| 20 × 13 × 10 | 102 s | 0.0223 | 96 s | 0.1364 |
| 45 × 32 × 23 | 642 s | 0.0165 | 543 s | 0.0436 |
| 60 × 49 × 34 | 1568 s | 0.0083 | 1367 s | 0.0243 |

Table 3 gives the corresponding simulation times and mean relative errors of WOFDM method and WKB-Wavelet method based on the number of grid points in x, y, z directions. We observe that for obtaining approximately the same precision, the simulation time is reduced significantly with the WKB-Wavelet method compared to WOFDM method. An extensive comparison of the surface potential values of nanoscale FinFET using WKB-Wavelet method shows that it approximates more accurately with less number of grid points than the FDM and WOFDM methods. Hence the simulation time is reduced considerably.

## 6. Conclusions

The WKB-Wavelet method for modeling nanoscale FinFET photodetector including quantum mechanical effects (QME) shows that the FinFET may retain performance acceptable for OEIC receiver applications even if the gate length is reduced to nanoscale with reduced computation time. It also shows the efficiency of the WKB-Wavelet method as compared to WOFDM and FDM methods. Accurate results have been obtained with significantly reduced computational time.

## References

[1] P. Chakrabarti, S. Kumar, P. K. Rout, B. G. Rappai, Proceeding 3rd Asia Pacific Microwave Conference, Tokyo, Japan, 1990, pp 575-578.
[2] P. Chakrabarti, I. Venugopal, Phys. Stat. Sol.(a) **147**, 277 (1995).
[3] K. Ohata, "InP MISFET", Workshop Digest., Asia Pacific Microwave Conference, Tokyo, Japan, pp 15-20, 1990
[4] P. Chakrabarti, B. K. Mishra, Y. Pratap Reddy, S. Prakash, Phys.Stat. Sol.(a), **147**, 277 (1995).
[5] K. Okamoto, S. Inoue, Solid-state Electronics, **16**, 657 (1973).
[6] M. Kabeer, K. Gowri, V. Rajamani, J. Optoelectron. Adv. Mater., **9**(9), 2879 (2007).
[7] J.-P. Colinge, Solid state Electron. **48**(6), 897 (2004).
[8] Y. Taur, L. H. Wann, D. J. Frank, "25nm CMOS design considerations," in IEDM Tech. Dig., pp. 789-792 (1998).
[9] Y. Taur, D. A. Buchanan, W. Chen, D. J. Frank, K. E. Ismail, S. -H. Lo, G. A. Sai-Halasz, R.G., Viswanathan, H.-J.C. Wann, S. J. Wind, H.-S.P Wong, Proc.IEEE, **85** (4) 486 (1997).
[10] D. J. Frank, R. H. Dennard, E. Nowak, Proc. IEEE **89**(3), 259 (2001).
[11] Y. Taur, "CMOS scaling beyond 0.1μm: how far can it go?" in Proc. Symp. VLSI Technology, pp. 6-9, 1999
[12] D. J. Frank, S. E. Laux, M. V. Fischetti, "Monte Carlo simulation of 30nm dual-gate MOSFET: how short can Si go?," in IEDM Tech. Dig., 1992, pp. 553-556.
[13] D. J. Frank, S. E. Laux, M. V. Fischetti, IEEE Trans. Electron Device **40**, 2103 (1993).
[14] R.-H. Yan, A. Ourmazd, K. F. Lee, IEEE Trans. Electron Devices, **39**, 1704 (1992).
[15] K. Suzuki, T. Tanaka, Y. Tasaka, H. Horie, Y. Arimato, IEEE Trans. Electron Devices **40**, 2326 (1993).
[16] H.-S.P.Wong, D. J. Frank, Y. Taur, J. M. C. Stork, in IEDM Tech. Dig., , pp. 747-750, 1994.
[17] H. -S. P. Wong, K. K. Chan, Y. Taur, "Self-aligned (top and bottom) double-gate MOSFET with a 25nm thick silicon channel ," in IEDM Tech. Dig., pp. 427-430, 1997
[18] J.-H. Lee, G. Taraschi, A. Wei, T. A. Langdo, E. A. Fitzgerald, D. A. Antoniadis, "Super self-aligned double-gate (SSDG) MOSFETs utilizing oxidation rate difference and selective epitaxy," in IEDM Tech. Dig., pp. 71-74, 1999.
[19] T. Su, J. P. Denton, G. W. Neudeck, New planar self-aligned double-gate fully depleted P-MOSFETs using epitaxial lateral overgrowth (ELO) and selectively grown source/drain (S/D)," in IEEE Int. SOI Conf., pp. 110-111, 2000.

[20] D. Hisamoto, W.-C. Lee, J. Kedzierski, H. Taeuchi, K. Asano, C. Kuo, R. Anderson, T.-J. King, J. Bokor, C. Hu, IEEE Trans. Electron Devices **47**, 2320 (2000).
[21] X. Huang, W.-C. Lee, C. Ion Kuo, D. Hisamoto, L. Chang, J. Kedzierski, R. Anderson, H. Takeuchi, Y.-K. Choi, K. Asano, V. Subramanian, V. King, J. Bokor, V. Hu, IEEE Trans. Electron Devices **48**, 880 (2001).
[22] Dnyanesh S. Havaldar, Guruprasad Katti, Nandita DasGupta, Amitava DasGupta, IEEE Trans. Electron Devices, **53**(4), 737 (2006).
[23] G. Pei, J. Kedzierski, P. Oldiges, M. Ieong, V. Chin-Chaun Kan, IEEE Trans.Electron Devices **49**(8), 1411 (2002).
[24] H. A. El Hamid, J. R. Guitart, V. Kilchytska, D. Flandre, B. Iniguez, IEEE Trans. Electron Devices, **54**(9), 2487 (2007).
[25] W. Yang, Z. Yu, L. Tian, IEEE Trans. Electron Devices, **54**(5), 1140 (2007).
[26] Xue Shao, Zhiping Yu, Solid-State Electronics, **49**, 1435 (2005).
[27] M. Lundstrom, J.-H Rhew, Journal of Computational Electronics, 1, pp. 481-489.
[28] D. Zhang, X. Shao, V. Yu, V. Tiang, Proc.SISPAD, pp. 195-198, 2005
[29] H. Khan, V. Mamaluy, V. Vasileska, Journal of Physics: Conf. series **38**, 196 (2006).
[30] V. Kedzierski, V. Fried, E. J. Nowak, V. Kanarsky, J. H. Rankin, H. Hanafi, W. Natzle, D. Boyd, Y. Zhang, V. Roy, J. Newbury, V. Yu, V. Yang, P. Saunders, C. P. Willets, A. Johnson, S. P. Cole, H. E. Young, N. Carpenter, D. Rakowski, B. A. Rainey, P. E. Coltrell, M. Leong, H.-S. Philip Wong, IEDM Tech. Dig., , pp 437 (2001).
[31] S. H. Tang, L. Chang, N. Lindert, Y.-K. Choi, W.-C. Lee, X. Huang, V. Subramanian, "FinFET –a quasiplanar double-gate MOSFET," in Proc. Int. Solid-State Circuits Conf. (ISSCC), 2001, pp. 118-119.
[32] D. M. Fried, A. P. Johnson, E. J. Nowak, J. H. Rankin, C. R. Willets, Proc. Device Res. Conf., 24, 2001.
[33] N. Ben Abdallah, M. Mouis, C.Negulescu, Journal of Computational Physics, **225**, 74 (2007).
[34] N. Ben Abdallah, O. Pinaud, Journal of Computational Physics **213**, 288 (2006).
[35] J. Wang, "Device Physics and Simulation of Silicon Nanowire Transistors ", Ph.D., Thesis, Purdue University, 2005.
[36] K. Kim, O. Kwon, J. Seo, T. Won, Japanese Journal of Applied Physics, **43**, 3784 (2004).
[37] L. De Marchi, F. Franze, E. Baravelli, Solid-state Electronics, **50**, 650 (2006).
[38] L. Jameson, , SIAM J SCI Comput. **19**(6), 1980 (1998).
[39] I. Fatkulin, J. S. Hesthaven ' Adaptive high-order finite-difference method for nonlinear wave problems' Scientific computing report series, 2001.
[40] M. Krumholz, L. P. B. Katehi, ,IEEE Trans. Microwave Theory Tech. **44**, 555 (1996).
[41] M. Tentzeris, J. Harvey, IEEE Microwave Guided Wave Lett. **9**, 96 (1999).
[42] Sebstien Goasguen, IEEE Trans on Microwave Theory and Techniques, **49**(12) 2258 (2001).
[43] Yasser A. Hussein, Samir M. El-Ghazaley, IEEE Trans. on Microwave Theory and Techniques, **51**(7), 1842 (2003).
[44] M. Toupikov, G. Pan, IEEE Trans. on Microwave Theory And Techniques **48**( 4), 500 (2000).
[45] M. Holmstron, SIAM J. Sci. Comp. **21**(2), 405 (1999).
[46] I. Daubechies, Ten Lectures on Wavelets, Capital city press , Vermont, 1992.
[47] S. Mallat, A. Wavelet, Tour of Signal Processing, Academic Press, NewYork, 1992.
[48] K. Amaratunga, J. R. Williams, Int. J. Numer. Methods. Eng. **37**, 2705 (1994).

*Corresponding author: ramesh24.dr@gmail.com